Control of plasma-CVD SiO_2/InAlN interface by ultrathin atomic-layer-deposited Al_2O_3 interlayer

Masamichi Akazawa[1*] and Shouhei Kitajima[1]

[1]*Research Center for Integrated Quantum Electronics, Hokkaido University, Sapporo 060-0813, Japan*

E-mail: akazawa@rciqe.hokudai.ac.jp

To control a plasma-CVD SiO_2/InAlN interface, the insertion of an ultrathin Al_2O_3 interlayer deposited by atomic layer deposition was investigated. The thickness of the Al_2O_3 interlayer was varied between 0.5 and 2 nm. Compared with the direct deposition of SiO_2, the insertion of a 2- or 1-nm-thick Al_2O_3 interlayer resulted in the similar interface state density D_{it} distribution. However, a significant reduction in D_{it} was achieved by using a 0.5-nm-thick Al_2O_3 interlayer. Slight oxidation of the InAlN surface under the 0.5-nm-thick Al_2O_3 interlayer was observed by X-ray photoelectron spectroscopy (XPS). This result indicated that a native oxide/InAlN interface was formed without disorder beneath the 0.5-nm-thick Al_2O_3 interlayer, while plasma damage was prevented at the interface. On the other hand, the density of positive charges at the interface increased with the Al_2O_3 interlayer thickness. The generation process of the interface charge is discussed on the basis of XPS data.

1. Introduction

GaN has a wide band gap, a high breakdown field, a high electron saturation velocity, and good thermal conductivity. These characteristics make GaN suitable for use in power electronics devices. In addition, by combining GaN with a III-nitride alloy to form a heterostructure, a high-mobility two-dimensional electron gas (2DEG) can be obtained in a high-electron-mobility transistor (HEMT). AlGaN/GaN HEMTs are actually used as high-power high-frequency devices to miniaturize high-power communication equipment. $In_xAl_{1-x}N$ (x = 0.17 – 0.18) lattice matched to GaN has a large band gap[1)] and a large spontaneous polarization[2)]. A lattice-matched InAlN/GaN heterostructure can provide a higher 2DEG density than an AlGaN/GaN heterostructure owing to the larger conduction band discontinuity and the larger interface polarization[3)]. In fact, a 2DEG density higher than 2×10^{13} cm^{-2} has been obtained and reported[4–10)]. Therefore, InAlN/GaN heterostructures are expected to construct HEMTs exhibiting excellent performance. However, the leakage current through an InAlN barrier is high owing to its large polarization, resulting in a high internal electric field that allows electron tunneling[11, 12)]. To solve this problem, the construction of a metal-insulator-semiconductor (MIS) gate structure has been proposed for InAlN/GaN HEMT applications[11)]. Thus far, combinations of InAlN and several insulators, including Al_2O_3[11, 13–17)], ZrO_2[14, 18, 19)], $GdScO_3$[14)], HfO_2[18)], SiO_2[20)], plasma oxides[21–25)], and thermal oxides[26, 27)], have been used to construct MIS gate structures to reduce the leakage current. Among these insulators, SiO_2 is attractive because it has the largest band gap among the insulators in practical use. Nevertheless, a method of controlling the SiO_2/InAlN interface to reduce the interface state density D_{it} has not been established.

For the deposition of the SiO_2 layer, plasma-CVD is a frequently used method. In this method, however, surface damage caused by plasma may result in the generation of interface states. We previously reported that the direct deposition of SiO_2 on InAlN by plasma CVD resulted in the surface oxidation of InAlN, which indicated that the surface was damaged by the plasma[28)]. According to the disorder-induced gap state (DIGS) model, the origin of the interface states is interface disorder[29)]. To reduce interface disorder caused by plasma damage, one of the useful methods is to insert an interface control layer. We reported that an ultrathin N_2O plasma oxide interlayer reduced D_{it} at the plasma-CVD SiO_2/InAlN interface compared with the case of the direct deposition[28)]. Therefore, the native oxide/InAlN interface is highly likely an excellent interface as long as the plasma damage during plasma CVD is blocked by the interlayer.

Since the native oxide of InAlN contains an Al oxide component, there is a possibility that the ultrathin native oxide interlayer can be replaced by an ultrathin Al_2O_3 layer carefully formed by atomic layer deposition (ALD) to control the SiO_2/InAlN interface. Although we also attempted to insert a 2-nm-thick ALD Al_2O_3 interlayer at the SiO_2/InAlN interface in our previous work[28], the reduction in D_{it} was not significant compared with that achieved by the insertion of the plasma native oxide interlayer. However, the thickness of the Al_2O_3 interlayer has not been optimized. Furthermore, in our previous work[28], we evaluated D_{it} by applying the Terman method to the measured capacitance–voltage (*C*–*V*) curves. However, the error caused by the Terman method is relatively large, especially for low D_{it} values.

In this work, we focused on the control of the plasma-CVD SiO_2/InAlN interface by inserting an ultrathin Al_2O_3 interlayer. Samples with 2-, 1-, and 0.5-nm-thick Al_2O_3 interlayer were fabricated and tested. The parameters related to the band alignment were measured by X-ray photoelectron spectroscopy (XPS). The *C*–*V* characteristics were simulated using these parameters to extract the D_{it} distributions from the experimental data. We found that the 0.5-nm-thick Al_2O_3 interlayer markedly reduced D_{it} at the plasma-CVD SiO_2/InAlN interface. The mechanism of the reduction in D_{it} is discussed on the basis of the results of XPS. In addition, the interface charge introduced by the insertion of an Al_2O_3 interlayer was investigated. The generation process of the interface charge was also studied and is discussed.

2. Experimental

For electrical measurements, MIS diodes, as shown in Fig. 1, were fabricated as follows. A Si-doped InAlN layer was grown by metal organic vapor phase epitaxy (MOVPE) on sapphire substrates via a GaN buffer layer. The carrier concentration, *n*, of the InAlN layer was 2×10^{18} cm^{-3} and the thickness was 160 nm, which enabled us to characterize the samples as ordinary MIS diodes without considering the 2DEG that was located much deeper than the depletion layer edge. Chemical treatment was carried out using buffered HF solution (BHF, NH_4F:HF=5:1) to remove the surface oxide. A 20-nm-thick SiN layer for protecting the InAlN surface during ohmic annealing was deposited by electron cyclotron resonance plasma CVD at 270°C with 100 W plasma power using a N_2 and SiH_4/Ar gas mixture. After photolithography and partial removal of SiN by BHF, a Ti (20 nm; bottom)/Al (50 nm)/Ni (20 nm)/Au (50 nm; topmost) ohmic contact was formed as a large pad perforated with a periodic-hole array. Subsequently, the sample was annealed at

850°C for 1 min using the SiN surface protection layer. After annealing, the SiN layer was removed by the BHF solution. The Al_2O_3 interlayer was formed by ALD at 300°C using trimethylaluminum and H_2O. The thickness of the Al_2O_3 interlayer was controlled by setting the deposition cycle number (0.12 nm/cycle). For comparison, a sample without an Al_2O_3 interlayer was also fabricated. SiO_2 was deposited by plasma-enhanced chemical vapor deposition (PECVD) at 300°C with 30 W plasma power using a N_2O and SiH_4 gas mixture. The thickness of the SiO_2 layer was controlled to be 20 ± 1 nm by adjusting the deposition time (6.7 nm/min). Finally, the Ni (20 nm; lower)/Au (50 nm; upper) circular gate electrode was formed in the center of the hole of the ohmic contact pad to complete the MIS structure.

The insulator/InAlN interface was examined by XPS using a sample with an ultrathin insulator layer deposited onto an undoped 30-nm-thick InAlN layer grown by MOVPE on a sapphire substrate via a 2-μm-thick GaN buffer layer. A monochromated Al-*K*α X-ray source (1486.6 eV) was used. The charge-up error in binding energy was calibrated by setting the C 1s spectral peak to 285.0 eV.

3. Results and discussion

We carried out XPS measurement of the band gap E_g and the valence band offset ΔE_V between plasma CVD SiO_2 and InAlN layers. On the basis of the energy difference between the core peak and the loss peak onset in the O 1s spectrum, E_g of the oxide layer can be measured[30]. The measured O 1s energy-loss spectrum for 30-nm-thick SiO_2 is shown in Fig. 2, where E_g of deposited SiO_2 was determined to be 8.6 ± 0.1 eV. This value is relatively smaller than the reported value for SiO_2[30]. This is presumably because of SiO_2 film quality, such as defects and content of nitrogen as described later, in addition to the measurement error. On the other hand, on the basis of the angle-resolved XPS for the valence band maximum (VBM) spectrum of the sample with 3-nm-thick SiO_2 on InAlN, we measured ΔE_V to be 2.3 ± 0.1 eV, as shown Fig. 3, where θ indicates the photoelectron take-off angle. Considering E_g of InAlN to be 4.6 eV[1], the conduction band offset ΔE_C was determined to be 1.7 eV. We used these values of E_g, ΔE_V, and ΔE_C as parameters for the SiO_2/InAlN interface in the simulation. In addition, the Schottky barrier height at the metal/SiO_2 interface was determined to be 3.7 eV, referring to the value measured by internal photoemission spectroscopy for Ni/thermal SiO_2 interface in Ref. 31. For the Al_2O_3/InAlN interface, the previously reported values of E_g = 6.7 eV for Al_2O_3[32], ΔE_V = 1.2 eV[16], and ΔE_C = 0.9 eV[16] were used. The band alignment assumed in the simulation is

illustrated in Fig. 4. Here, the dipole at the SiO_2/Al_2O_3 interface was ignored for simplicity.

The *C–V* curves measured at 1 MHz for the samples without and with 2-, 1-, and 0.5-nm-thick Al_2O_3 interlayers are plotted by the solid lines in Fig. 5. We carried out a simulation of *C–V* curves under assumption of a D_{it} distribution by choosing parameters, as described later, to make a best fit to the measured curves using a simulator developed previously[33, 34]. In Fig. 5, the simulated curves and the ideal curves were also shown by the open circles and the one-dot-chain lines, respectively. Here, the ideal curves were calculated assuming no charge at the interface and shifted to overlap on the measured curves in the deep depletion region, while the measured curves were not shifted. The voltage shift ΔV for each ideal curve is listed for each sample in Table I with the thicknesses of Al_2O_3 and SiO_2. A slight increase in oxide capacitance C_{ox} of the sample with the 0.5-nm-thick Al_2O_3 interlayer compared with that of the sample without the Al_2O_3 interlayer was resulted from the thinner SiO_2 layer thickness due to the thickness control error. On the other hand, ΔV is given by

$$\Delta V = \frac{1}{C_{ox}}\left(Q_{pol} + Q_f + Q_{it}^{fr}\right), \quad (1)$$

where Q_{pol} is the density of the polarization charge at the InAlN surface, Q_f is the density of the interfacial fixed charge, and Q_{it}^{fr} is the charge density of 'frozen' interface states with long time constants. Q_f may include the contribution of the oxide bulk charge. For the samples with the 0.5-nm-thick Al_2O_3 interlayer, the maximum capacitance was the closest to C_{ox} and the slope of the *C–V* curve was the largest among all samples, which indicated the largest and steepest shift of the surface Fermi level E_{FS} to E_C due to a decrease in D_{it}. Figure 6 summarizes the D_{it} distributions extracted from the *C–V* curves by the simulation, which were used to fit the measured curves for samples with various interlayer thicknesses. In the simulation, we assumed the D_{it} distribution based on the DIGS model[29]. According to this model, the interface states were originated from interface disorder resulting in a U-shaped D_{it} distribution in the bad gap. It is reported that the D_{it} distributions of III-nitride MIS diodes can be appropriately assumed as[33, 34]

$$D_{it}(E) = D_{it0} exp\left(\left|\frac{E-E_{CNL}}{E_{0D,0A}}\right|^{n_D,n_A}\right), \quad (2)$$

where D_{it0} is the minimum of D_{it}, E_{CNL} is the charge neutrality level, E_{0D} and n_D are the curvature factors assumed for the donor-like states below E_{CNL}, and E_{0A} and n_A are those for the acceptor-like states above E_{CNL}. E_{CNL} was assumed to be located 2.0 eV below the conduction band minimum energy, E_C[16]. Based on the *C–V* curves of n-type MIS diode, E_{0D} and n_D cannot be determined because the response of the interface states located below E_{CNL} becomes too slow. Here, D_{it0}, E_{0A}, and n_A are used as fitting parameters and determined as shown in Table II. E_{0A}, and n_A mainly affect the curvature of the *C–V* curves at the accumulation region, while D_{it0} dominantly affects the steepness in the depletion region. Since the difference of 10% in this parameter results in a deviation from the measured curve, the estimation accuracy of D_{it0} is empirically determined to be 10% as a fitting parameter. As shown in Fig. 6, the insertion of the 2- and 1-nm-thick Al_2O_3 interlayers led to the similar D_{it} distribution as that of the sample without interlayer. Nevertheless, the samples with the 0.5-nm-thick Al_2O_3 interlayer exhibited markedly reduced D_{it}. In the simulation, we also assumed a charge density, Q'_f, given by

$$Q'_f = Q_{pol} + Q_f \tag{3}$$

at the insulator/InAlN interface in addition to the D_{it} distribution. The assumed Q_f ($= Q'_f - Q_{pol}$) for each sample is plotted in Fig. 7 as a function of the thickness of the Al_2O_3 interlayer. Q_{pol} was assumed to be 2.88×10^{13} cm^{-2} according to Ref. 2. It can be seen, as a rough trend, that the increase in Al_2O_3 thickness led to the increase in the assumed positive Q_f. The mechanism of this result is discussed later.

To investigate the chemical bonding at the interface, the XPS study was carried out. Figure 8 shows XPS spectra after depositing a 3-nm-thick SiO_2 layer onto the samples with a 1-nm-thick Al_2O_3 interlayer. The O 1s and Al 2p spectra show the existence of an Al_2O_3 component, which indicates the successful formation of the Al_2O_3 interlayer. The higher energy component in the N 1s spectrum may be assigned to a small amount of SiON component[35, 36] in the SiO_2 layer because this component having the similar intensity ratio to that of the main peak was also observed for a 30-nm-thick SiO_2 layer by a separate experiment. Since the shape of the N 1s spectra after Al_2O_3 deposition was coincident with that before Al_2O_3 deposition (not shown here), it is unlikely that the Al_2O_3 layer turned into an AlON layer because of intermixing. Actually, the lower binding energy component at 531 eV in the O 1s spectra in Fig. 8 (a) is assigned to Al_2O_3[37,38]. On the other hand, the In 3d spectrum does not show the oxide component, indicating that there was no oxidation

of the InAlN surface. As plotted in Fig. 9, however, the In 3d spectrum from the sample with a 0.5-nm-thick Al_2O_3 interlayer after the SiO_2 deposition shows an oxide component. To clarify the difference, the In 3d spectra in Figs. 8 (b) and 9 (b) are compared in Fig. 10, where the intensity was normalized and the spectrum of the sample with the 1-nm-thick Al_2O_3 interlayer was shifted horizontally for overlapping. It can be seen that the spectra for the sample with the 0.5-nm-thick layer is wider. (In O1s spectrum, it is difficult to confirm the existence of the In-oxide component because its intensity should be less than that of the hem of the SiO_2 component indicated by a Voigt function, considering the In molar fraction of InAlN and the thinness of the oxidized layer.) Thus, the InAlN surface of the sample with the 0.5-nm-thick Al_2O_3 interlayer was oxidized during the deposition of SiO_2 by PECVD. Slight oxidation during the deposition of SiO_2 beneath the sub-nm-thickness Al_2O_3 interlayer led to the formation of a native oxide/InAlN interface. Plasma damage during SiO_2 deposition presumably caused by the stochastic collisions of ions to the InAlN surface can lead to interface disorder by changing connection, length and angle of the chemical bonds at the interface. Considering the electrical measurement results, it is highly likely that the oxidation beneath the Al_2O_3 interlayer proceeded without causing disorder. Therefore, it is also likely that the native oxide/InAlN interface was protected from plasma damage by the 0.5-nm-thick Al_2O_3 interlayer as a result of a mechanism where the penetration depth of the oxidizing species was greater than that of the damaging species. This result indicated that the native oxide/InAlN interface has excellent properties if it is formed appropriately so as to prevent plasma damage.

In this work, the InAlN layers of the present samples were grown on sapphire substrate. Therefore, an exact determination of the E_{FS} position by XPS is difficult. Nevertheless, since the binding energy was calibrated by the C 1s peak position, the core-level energy at each step of the interface formation can be a rough reference of the charging situation at the InAlN surface. Actually, the core-level spectra exhibited a remarkable change in binding energy. Figure 11 plots the peak binding energy of the InAlN component of the Al 2p spectrum, $E_{\mathrm{Al\ 2p\ InAlN}}$, at each step of interface formation. Direct deposition of an ultrathin SiO_2 layer onto the InAlN surface resulted in an increase of $E_{\mathrm{Al\ 2p\ InAlN}}$. However, after the deposition of an Al_2O_3 layer, $E_{\mathrm{Al\ 2p\ InAlN}}$ decreased. The present result indicates an increase in the amount of negative charge in the vicinity of the surface upon the deposition of the Al_2O_3 layer onto InAlN. However, $E_{\mathrm{Al\ 2p\ InAlN}}$ increased after the subsequent SiO_2 deposition, which indicated a decrease in or compensation for the negative charge in the vicinity of the surface of the tested samples. Therefore, the

negative charge observed for the ultrathin Al_2O_3/InAlN structure might have existed at the topmost surface of the Al_2O_3 layer. These changes were commonly observed for the samples with 1-nm-thick and 0.5-nm-thick Al_2O_3 interlayer. In addition, the similar changes were observed also in In 3d and N 1s spectra.

Fig. 12 shows the result of the angle-resolved XPS for the O 1s spectrum from the 2-nm-thick Al_2O_3/InAlN structure. The ratio of the intensity of the higher-energy-component of the O 1s spectrum, which is usually assigned to Al–O–H bonding[37, 38], to that of the Al–O–Al component[37, 38] at the lower binding energy increased as the take-off angle decreased. This result can be explained by the localization of H-terminated oxygen dangling bonds at the surface of the ultrathin Al_2O_3 layer. This is natural considering that the layer-by-layer growth was interrupted at the surface of the ALD Al_2O_3 layer. However, statistically, the termination by hydrogen might be absent in part of the dangling bonds. According to previous calculation results[39], an oxygen dangling bond generates an acceptor-like level near the VBM (E_V + 0.9eV) in α-Al_2O_3, which has a local environment similar to that of amorphous Al_2O_3. This level can behave as a negative fixed charge, considering the aforementioned ΔE_V (1.2 eV) between Al_2O_3 and InAlN. After the subsequent SiO_2 deposition, such oxygen dangling bonds were possibly recovered to minimize the negative charge, resulting in the dominance of the residual positive charge at the Al_2O_3/InAlN interface of the completed MIS diodes.

Although it is desirable to confirm the existence of the hydroxide component also in Al 2p spectra, the separation of oxide and hydroxide components in Al 2p spectra is difficult by the reason as follows. The topmost Al atoms of the Al_2O_3 layer before SiO_2 deposition were possibly connected as HO–$\underline{\text{Al}}$(–O–Al)$_2$, and those in bulk Al_2O_3 were connected as $\underline{\text{Al}}$(–O–Al)$_3$. Therefore, the binding energy of these components in Al 2p spectrum should be close each other due to the similar local chemistry[38]. Actually, the Al 2p binding energy is reported to be very similar between Al_2O_3 and hydroxides[40]. Even in Ref. 38 where the native oxides on the Al metal surface was investigated by XPS in detail, components from Al atoms in Al_2O_3 and AlO(OH) were not separated in the Al 2p spectra.

The increase in positive charge with the Al_2O_3 interlayer thickness shown in Fig. 7 for the completed MIS diodes might have existed in the bulk Al_2O_3 because the interface quality affected on Q_{it}^{fr} that was separated from Q_f in the simulation. On the basis of a separate experiment, Q_f was 2.54×10^{13} cm^{-2} for a metal/Al_2O_3 (20 nm)/InAlN MIS diode prepared for comparison. Although the similar generation of the positive interface charge

has been reported for an Al_2O_3/GaN interface[41], Q_f was 2.27×10^{13} cm^{-2}. Therefore, 2.88×10^{13} cm^{-2} of Q_f observed for the MIS diode with the 2-nm-thick Al_2O_3 interlayer was higher than these values, which indicates that the volume density of the bulk positive charge in the Al_2O_3 interlayer should have been higher than the thick Al_2O_3 layer. This may be a phenomenon that was induced by the plasma irradiation. In Ref. 39, the possibility that the origin of the positive charge is aluminum interstitials was discussed because they generate donor-like defects near the conduction band of α-Al_2O_3. However, E_g of α-Al_2O_3 was calculated to be 9.2 eV[39], which is different from that (6.7 eV) measured for amorphous ALD Al_2O_3[32]. Therefore, the dominant defect in the Al_2O_3 interlayer is unclear at this stage. Recently, post-metallization annealing in air has been found to be an efficient means of reducing D_{it} and the positive charge owing to the Al_2O_3 bulk defects in the metal/ALD Al_2O_3/GaN MIS structure[42]. It is worth finding a method of reducing the positive charge in the Al_2O_3 interlayer, which is future work.

4. Conclusions

The control of plasma-CVD SiO_2/InAlN interfaces by using an ALD Al_2O_3 interlayer was investigated. The thickness of the Al_2O_3 interlayer was set to 2, 1, and 0.5 nm. Compared with the direct deposition of SiO_2 onto an InAlN surface, the insertion of the 2- or 1-nm-thick Al_2O_3 interlayer resulted in the similar D_{it} distribution. However, a significant reduction in D_{it} was achieved by using the 0.5-nm-thick Al_2O_3 interlayer. It is highly likely that the oxidation beneath the 0.5-nm-thick Al_2O_3 interlayer proceeded without causing disorder because the native oxide/InAlN interface was protected from plasma damage, presumably because the penetration depth of the oxidizing plasma species was greater than that of the damaging species. That is, the formation of a plasma native oxide/InAlN interface without damage led to the reduction in D_{it}. On the other hand, the Al_2O_3 interlayer was found to introduce positive charge at the SiO_2/InAlN interface. The generation process of the interface charge was also studied and discussed.

Acknowledgement

This work was supported by JSPS KAKENHI Grant Number JP15K04672 and JP16H06421.

References

1) R. E. Jones, R. Broesler, K. M. Yu, J. W. Ager III, E. E. Haller, W. Walukiewicz, X. Chen and W. J. Schaff, J. Appl. Phys. **104**, 123501 (2008).
2) O. Ambacher, R. Dimitrov, M. Stutzmann, B. E. Foutz, M. J. Murphy, J. A. Smart, J. R. Shealy, N. G. Weimann, K. Chu, M. Chumbes, B. Green, A. J. Sierakowski, W. J. Schaff and L. F. Eastman, Phys. Status Solidi B **216**, 381 (1999).
3) J. Kuzmík, IEEE Electron. Device Lett. **22**, 510 (2001).
4) M. Higashiwaki and T. Matsui, Jpn. J. Appl. Phys. **43**, L768 (2004).
5) J. Kuzmík, A. Kostopoulos, G. Konstantinidis, J.-F. Carlin, A. Georgakilas and D. Pogany, IEEE Electron. Device Lett. **53**, 422 (2006).
6) M. Gonschorek, J.-F. Carlin, E. Feltin, M. A. Py and N. Grandjean, Appl. Phys. Lett. **89**, 062106 (2006).
7) J. Xie, X. Ni, M. Wu, J. H. Leach, Ü. Özgür and H. Morkoç, Appl. Phys. Lett. **91**, 132116 (2007).
8) M. Hiroki, N. Maeda and T. Kobayashi, Appl. Phys. Exp. **1**, 111102 (2008).
9) M. Gonschorek, J.-F. Carlin, E. Feltin, M. A. Py, N. Grandjean, V. Darakchieva, B. Monemar, M. Lorenz and G. Ramn, J. Appl. Phys. **103**, 093714 (2008).
10) L. Ardaravičius, M. Ramonas, J. Liberis, O. Kiprijanovič, A. Matulionis, J. Xie, M. Wu, J. H. Leach and H. Morkoç, J. Appl. Phys. **106**, 073708 (2009).
11) G. Pozzovivo, J. Kuzmík, S. Golka, W. Schrenk, G. Strasser, D. Pogany, K. Ĉiĉo, M. Ťapajna, K. Fröhlich, J.-F. Carlin, M. Gonschorek, E. Feltin and N. Grandjean, Appl. Phys. Lett. **91**, 043509 (2007).
12) J. Kotani Atsushi Yamada, Tetsuro Ishiguro, Shuichi Tomabechi and Norikazu Nakamura, Appl. Phys. Lett. **108**, 152109 (2016).
13) K. Čičo, J. Kuzmík, J. Liday, K. Hušeková, G. Pozzovivo, J.-F. Carlin, N. Grandjean, D. Pogany, P. Vogrinčič and K. Fröhlich, J. Vac. Sci. Technol. **B27**, 218 (2009).
14) K. Čičo, K. Hušeková, M. Ťapajna, D. Gregušová, R. Stoklas, J. Kuzmík, J.-F. Carlin, N. Grandjean, D. Pogany and K. Fröhlich, J. Vac. Sci. Technol. **B29**, 01A808 (2011).
15) M. Ťapajna, K. Čičo, J. Kuzmík, D. Pogany, G. Pozzovivo, G. Strasser, J.-F. Carlin, N. Grandjean and K. Fröhlich, Semicond. Sci. Technol. **24**, 035008 (2009).
16) M. Akazawa, M. Chiba and T. Nakano, Appl. Phys Lett. **102**, 231605 (2013).
17) S. Ozaki, K. Makiyama, T. Ohki, N. Okamoto, S. Kaneki, K. Nishiguchi, N. Hara, and T. Hashizume, Appl. Phys. Express **10**, 061001 (2017).
18) J. Kuzmík, G. Pozzovivo, S. Abermann, J.-F. Carlin, M. Gonschorek, E. Feltin, N.

Grandjean, E. Bertagnolli, G. Strasser and D. Pogany, IEEE Trans. Electron Devices **55**, 937 (2008).

19) P. Kordoš, R. Stoklas, D. Gregušová, K. Hušeková, J.-F. Carlin and N. Grandjean, Appl. Phys. Lett. **102**, 063502 (2013).

20) M. Lachab, M. Sultana, Q. Fareed, F. Husna, V. Adivarahan and A. Khan, J. Phys. D: Appl. Phys. **47**, 135108 (2014).

21) D. S. Lee, X. Gao, S. Guo and T. Palacios, IEEE Electron Device Lett. **32**, 617 (2011).

22) D. S. Lee, J. W. Chung, H. Wang, X. Gao, S. Guo, P. Fay and T. Palacios, IEEE Electron Device Lett. **32**, 755 (2011).

23) D. S. Lee, X. Gao, S. Guo, D. Kopp, P. Fay and T. Palacios, IEEE Electron Device Lett. **32**, 1525 (2011).

24) Y. Yue, Z. Hu, J. Guo, B. Sensale-Rodriguez, G. Li, R. Wang, F. Faria, T. Fang, B. Song, X. Gao, S. Guo, T. Kosel, G. Sinder, P. Fay, D. Jena and H. Xing, IEEE Electron Device Lett. **33**, 988 (2012).

25) Y. Yue, Z. Hu, J. Guo, B. Sensale-Rodriguez, G. Li, R. Wang, F. Faria, B. Song, X. Gao, S. Guo, T. Kosel, G. Sinder, P. Fay, D. Jena and H. Xing, Jpn. J. Appl. Phys. **52**, 08JN14 (2013).

26) M. Eickelkamp, M. Weingarten, L. Rahimzadeh Khoshroo, N. Katteniss, H. Behmenburg, M.Heuken, D. Donoval, A. Chvála, P. Kordoš, H. Kalisch and A. Vescan, J. Appl. Phys. **110**, 084501 (2011).

27) S. Ozaki, K. Makiyama, T. Ohki, Y. Kamada, M. Sato, Y. Niida, N. Okamoto and K. Joshin, Phys. Status Solidi A **213**, 1259 (2015).

28) M. Akazawa and A. Seino, Phys. Status Solidi B **254**, 1600691 (2017).

29) H. Hasegawa and H. Ohno, J. Vac. Sci. & Technol. B **4**, 1130 (1986).

30) S. Miyazaki, J. Vac. Sci. Technol. B **19**, 2212 (2001).

31) V. V. Afanas'ev, M. Houssa, A. Stesmans, and M. M. Heyns, J. Appl. Phys. **91**, 3079 (2002).

32) Y. Hori, C. Mizue, and T. Hashizume, Jpn. J. Appl. Phys. **49**, 080201 (2010).

33) M. Miczek, C. Mizue, T. Hashizume and B. Adamowicz, J. Appl. Phys. **103**, 104510 (2008).

34) M. Miczek, B. Adamowicz, C. Mizue and T. Hashizume, Jpn. J. Appl. Phys. **48**, 04C092 (2009).

35) S. M. Castanho, R. Moreno and J. L. G. Fierro, J. Mater. Sci. **32**, 157 (1997).

36) K. Kawase, J. Tanimura, H. Kurokawa, K. Kobayashi, A. Teramoto, T. Ogata and M.

Inoue, Mater. Sci. Semicond. Process. **2**, 225 (1999).

37) O. Renault, L. G. Gosset, D. Rouchon and A. Ermolieff, J. Vac. Sci. Technol. A **20,** 1867 (2002).

38) M. R. Alexander, G. E. Thompson and G. Beamson, Surf. Interface Anal. **29,** 468 (2000).

39) M. Choi, A. Janotti and C. G. Van de Walle, J. Appl. Phys. **113**, 044501 (2013).

40) D. Briggs and M. P. Seah, *Practical Surface Analysis by Auger and X-ray Photoelectron Spectroscopy*, Appendix 4, (John Wiley & Sons Ltd., Sussex, 1983).

41) M. Esposto, S. Krishnamoorthy, D. N. Nath, S. Bajaj, T.-H. Hung and S. Rajan, Appl. Phys. Lett. **99**, 133503 (2011).

42) S. Kaneki, J. Ohta, S. Toiya, Z. Yatabe, J. T. Asubar and T. Hashizume, Appl. Phys. Lett. **109**, 162104 (2016).

Figure Captions

Fig. 1. Structure of tested MIS diodes.

Fig. 2. XPS O 1s energy-loss spectra for the thick plasma-CVD SiO_2 layer.

Fig. 3. Take-off angle dependence of XPS VBM spectrum for 3-nm-thick SiO_2/InAlN sample.

Fig. 4. Band alignment assumed in the simulation of *C–V* characteristics.

Fig. 5. *C–V* characteristics. The solid lines are measured curves. The one-dot-chain lines are ideal curves. The open circles show the simulated curves assuming interface states to fit the measured curves. (a) Sample without Al_2O_3 interlayer. (b) Sample with 2-nm-thick Al_2O_3 layer. (c) Sample with 1-nm-thick Al_2O_3 layer. (d) Sample with 0.5-nm-thick Al_2O_3 layer.

Fig. 6. Evaluated D_{it} distributions.

Fig. 7. Assumed Q_f as a function of the thickness of the Al_2O_3 interlayer.

Fig. 8. XPS spectra for SiO_2 (3 nm)/Al_2O_3 (1 nm)/InAlN. (a) O 1s, (b) In 3d, (c) N 1s, and (d) Al 2p.

Fig. 9. XPS spectra for SiO_2 (3 nm)/Al_2O_3 (0.5 nm)/InAlN. (a) O 1s, (b) In 3d, (c) N 1s, and (d) Al 2p.

Fig. 10. Comparison of XPS In 3d spectra between samples with 1-nm-thick and 0.5-nm-thick Al_2O_3 interlayer.

Fig. 11. Binding energy of InAlN component in Al 2p spectra measured by XPS at each step of interface formation.

Fig. 12. Take-off angle dependence of O 1s spectrum for 2-nm-thick Al_2O_3 on InAlN.

Table I. Al_2O_3 and SiO_2 thicknesses and ideal curve shift ΔV for each sample.

Thickness of Al_2O_3 interlayer [nm]	Thickness of SiO_2 layer [nm]	ΔV [V]
0	20.4	3.15
0.5	19.8	2.55
1	20.7	2.15
2	20.8	0.95

Table II. Parameters relating to *D*it distribution used in simulation of *C*–*V* curve for each sample.

Thickness of Al_2O_3 interlayer [nm]	D_{it0} [$cm^{-2}eV^{-1}$]	n_A	E_{0A} [eV]
0	1.3×10^{12}	9.7	1.572
0.5	1.0×10^{11}	13.5	1.703
1	1.0×10^{12}	6.8	1.584
2	1.1×10^{12}	6.5	1.571

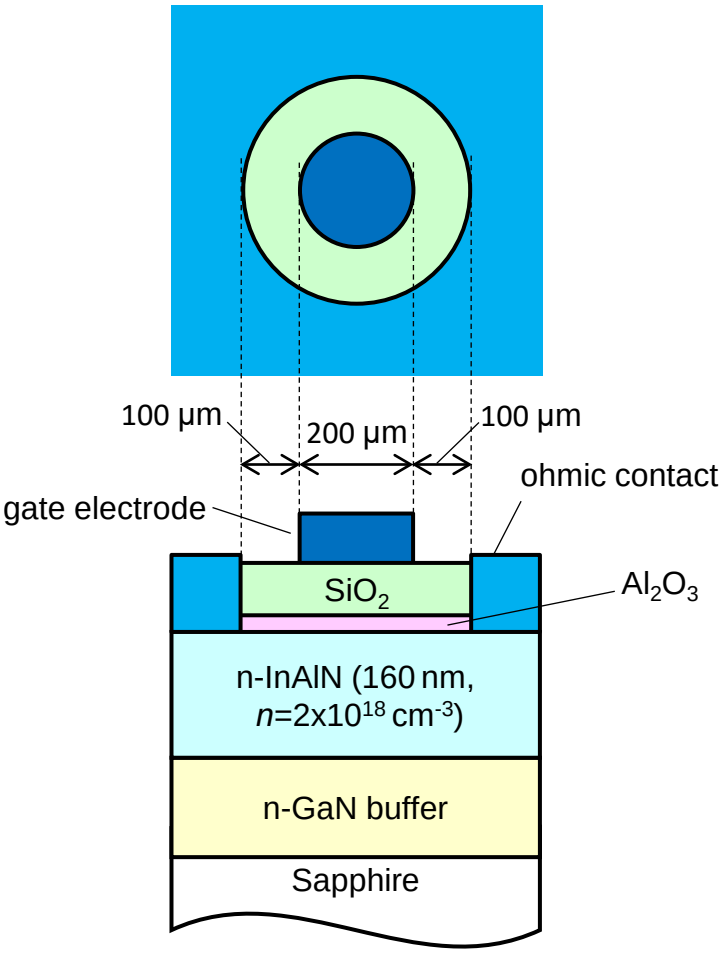
100 μm
200 μm
100 μm
ohmic contact
gate electrode
SiO2
Al2O3
n-InAlN (160 nm,
n=2x10^18 cm^-3)
n-GaN buffer
Sapphire

Fig. 1

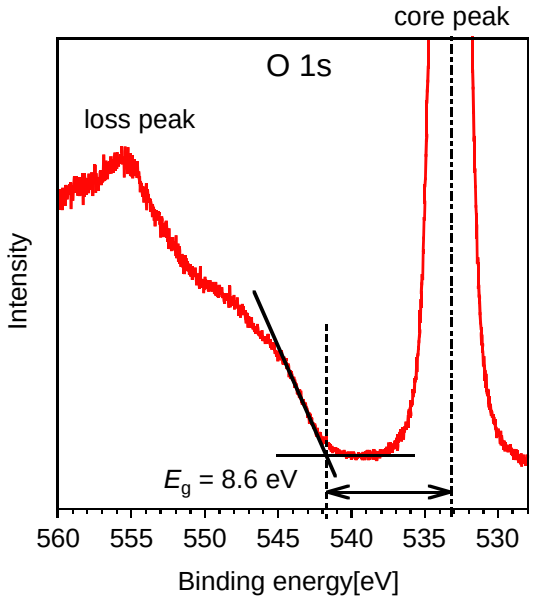
core peak
O 1s
loss peak
Intensity
Eg = 8.6 eV
560
555
550
545
540
535
530
Binding energy[eV]

Fig. 2.

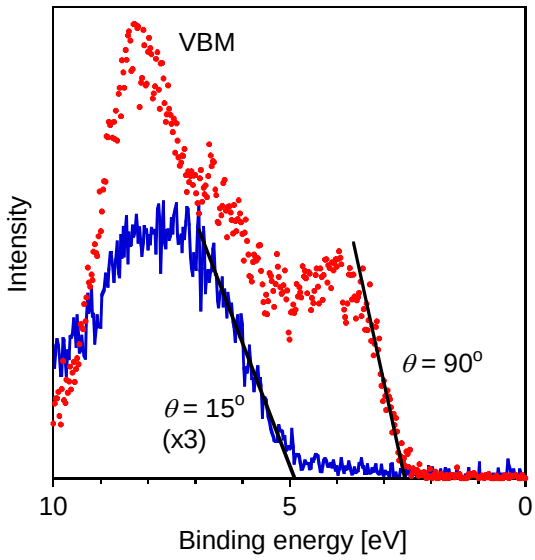
VBM
Intensity
θ = 90°
θ = 15°
(x3)
10
5
0
Binding energy [eV]

Fig. 3.

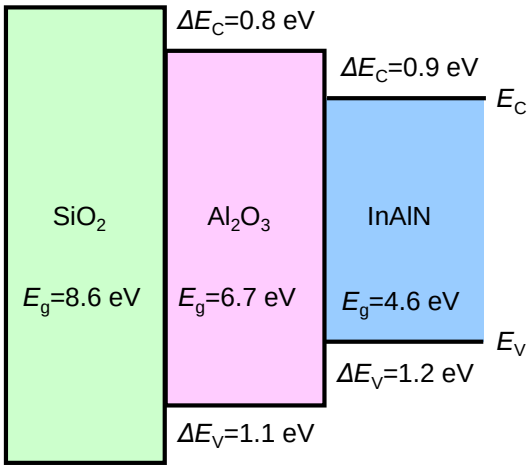
ΔE_C=0.8 eV
ΔE_C=0.9 eV
E_C
SiO2
Al2O3
InAlN
E_g=8.6 eV
E_g=6.7 eV
E_g=4.6 eV
E_V
ΔE_V=1.2 eV
ΔE_V=1.1 eV

Fig. 4.

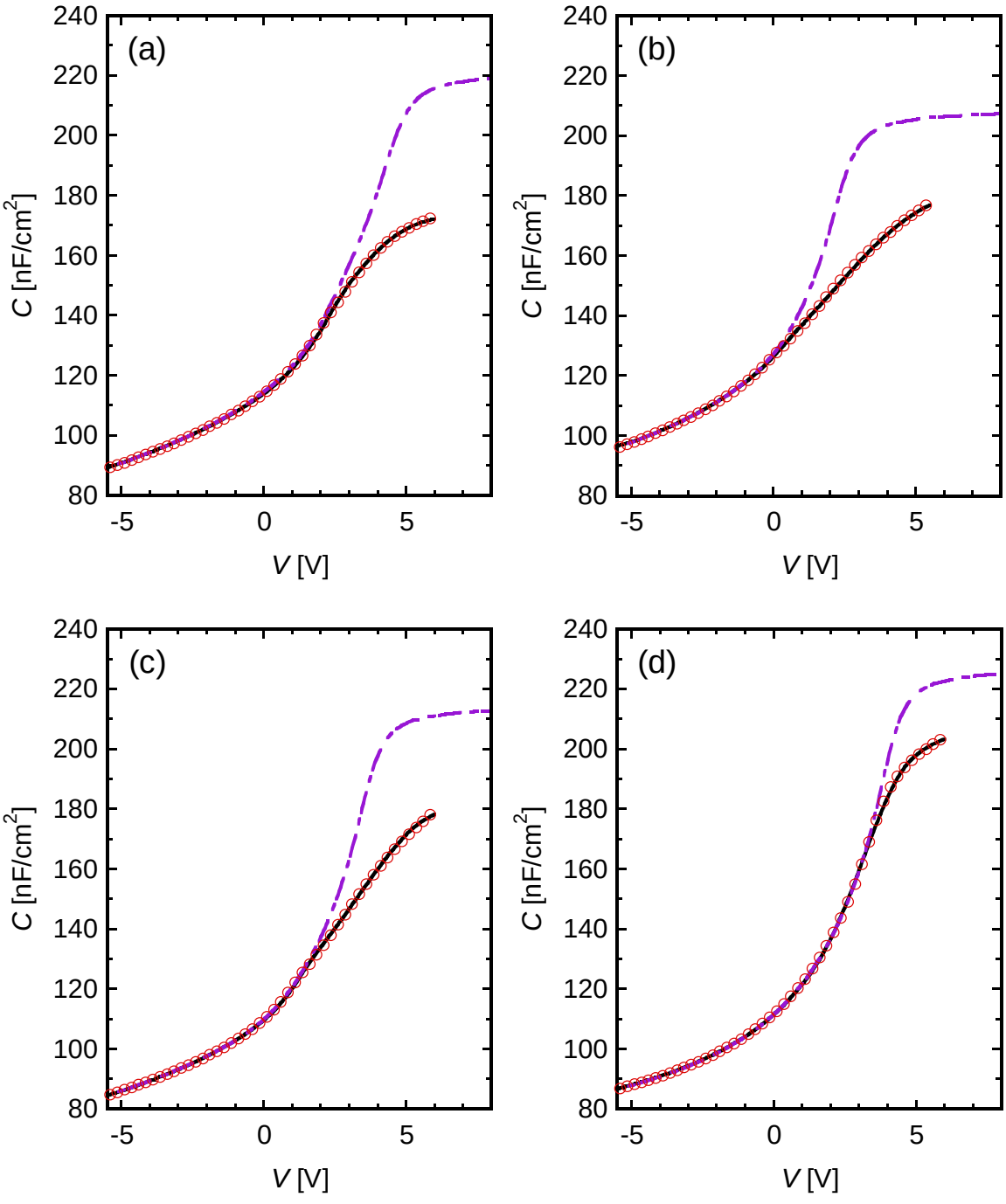

Fig. 5.

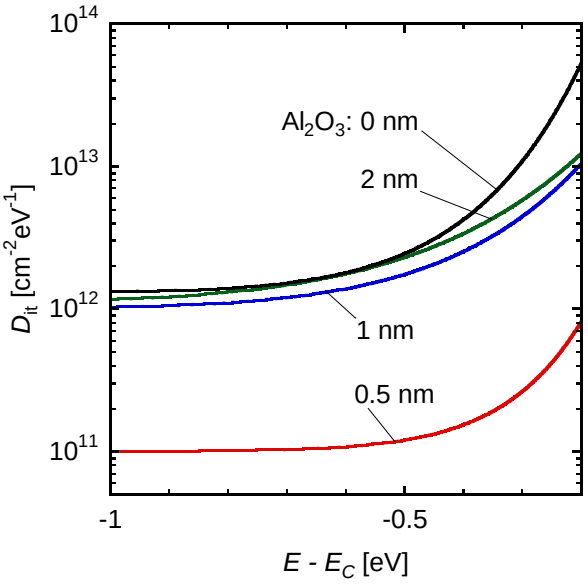
10^{14}
10^{13}
10^{12}
10^{11}
D_{it} [cm^{-2}eV^{-1}]
Al_2O_3: 0 nm
2 nm
1 nm
0.5 nm
-1
-0.5
E - E_C [eV]

Fig. 6.

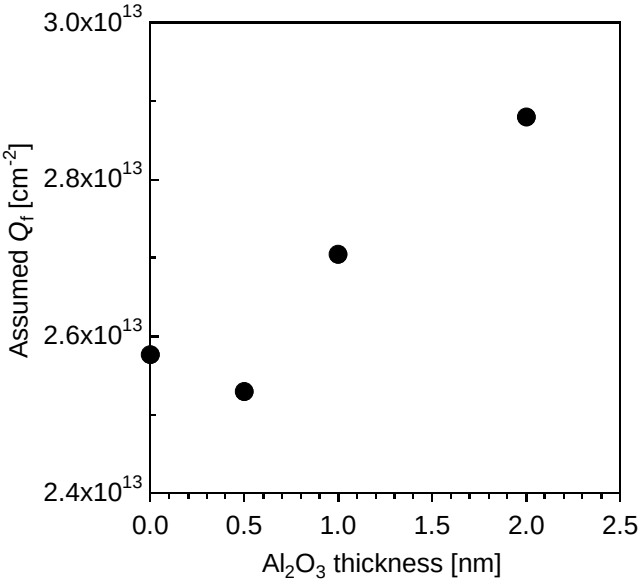
3.0x10^{13}
2.8x10^{13}
2.6x10^{13}
2.4x10^{13}
Assumed Q_f [cm^{-2}]
0.0
0.5
1.0
1.5
2.0
2.5
Al_2O_3 thickness [nm]

Fig.7.

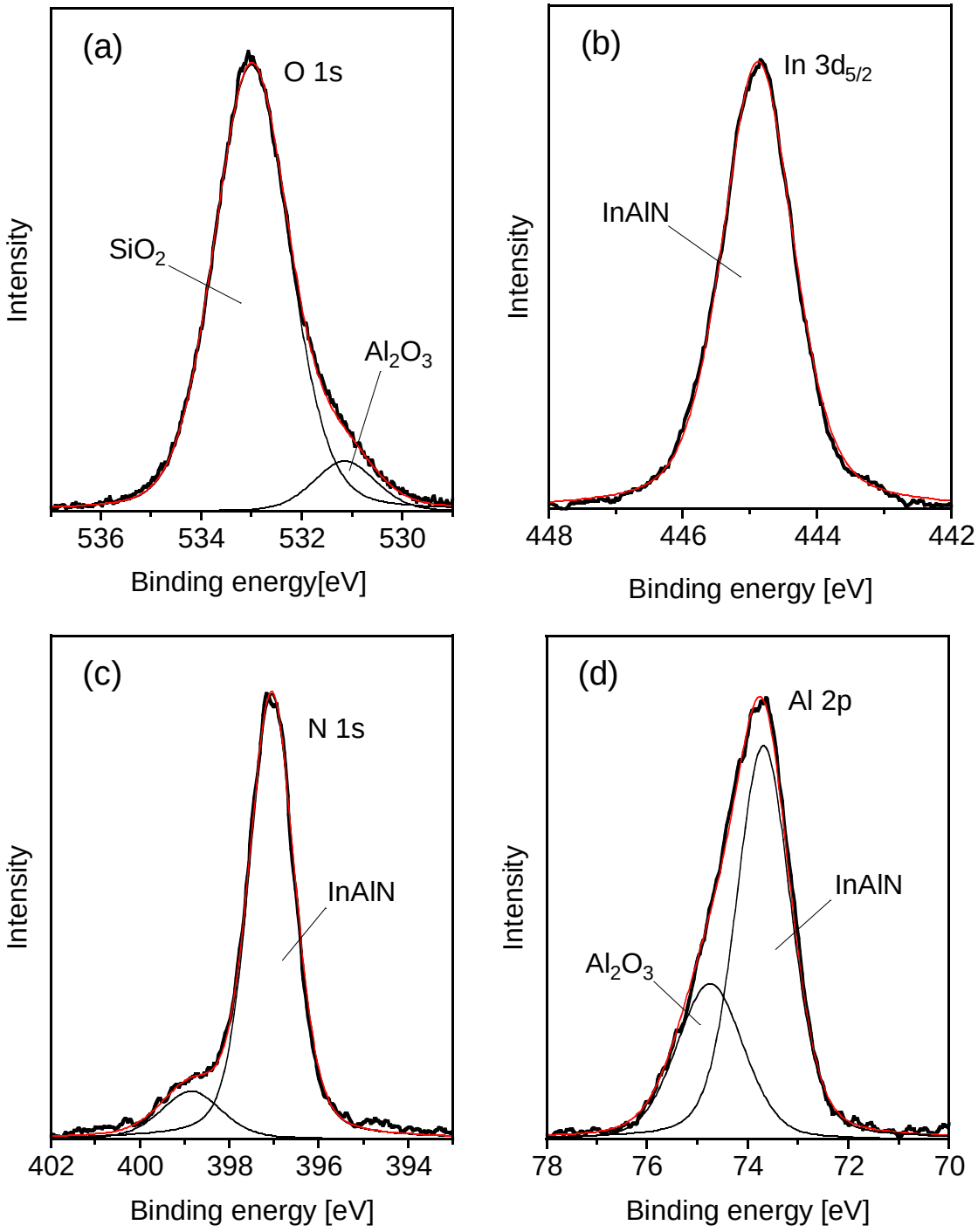
(a)
O 1s
SiO2
Al2O3
Intensity
536
534
532
530
Binding energy[eV]
(b)
In 3d5/2
InAlN
Intensity
448
446
444
442
Binding energy [eV]
(c)
N 1s
InAlN
Intensity
402
400
398
396
394
Binding energy [eV]
(d)
Al 2p
InAlN
Al2O3
Intensity
78
76
74
72
70
Binding energy [eV]

Fig. 8.

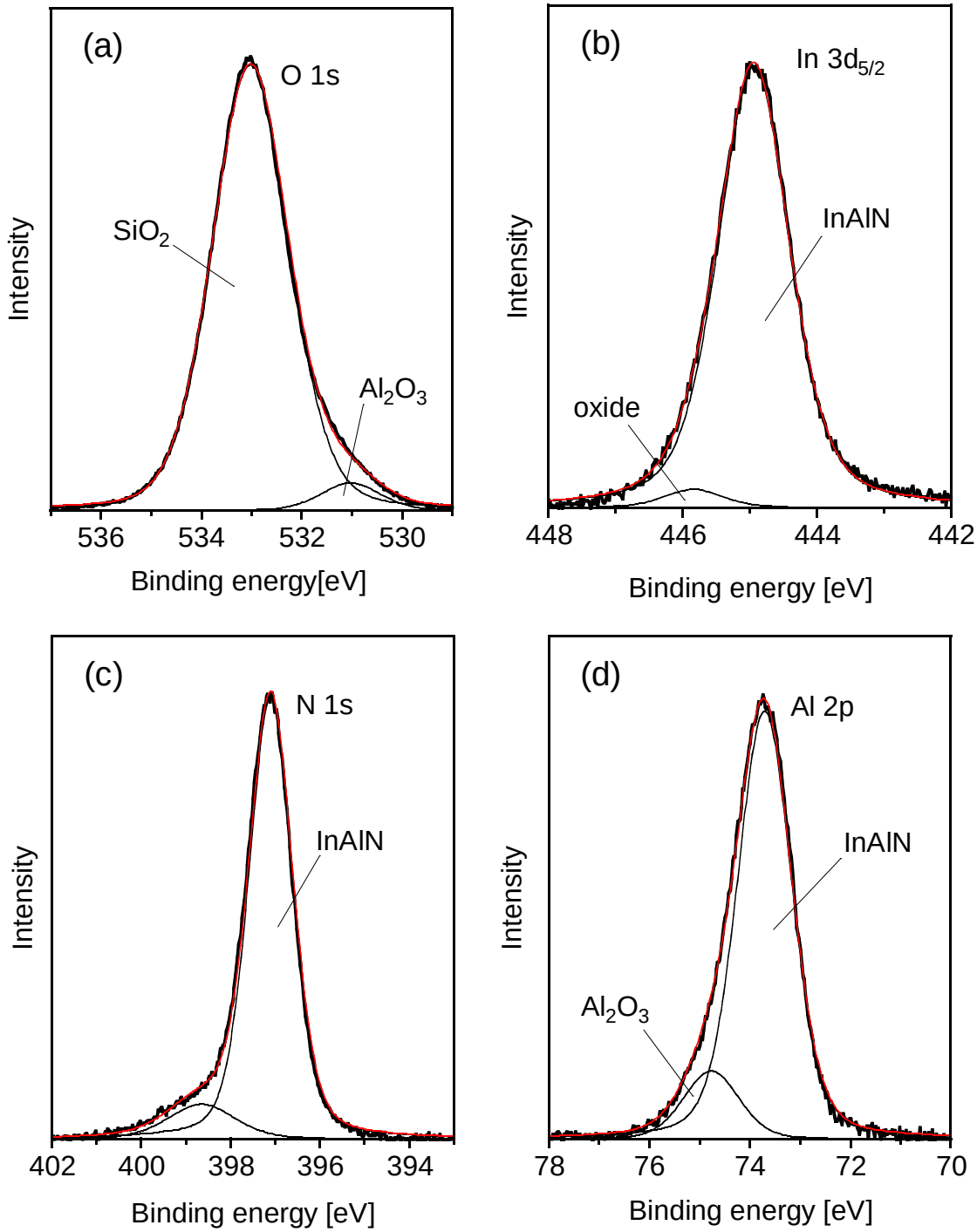
(a)
O 1s
SiO2
Al2O3
Intensity
536
534
532
530
Binding energy[eV]
(b)
In 3d5/2
InAlN
oxide
Intensity
448
446
444
442
Binding energy [eV]
(c)
N 1s
InAlN
Intensity
402
400
398
396
394
Binding energy [eV]
(d)
Al 2p
InAlN
Al2O3
Intensity
78
76
74
72
70
Binding energy [eV]

Fig. 9.

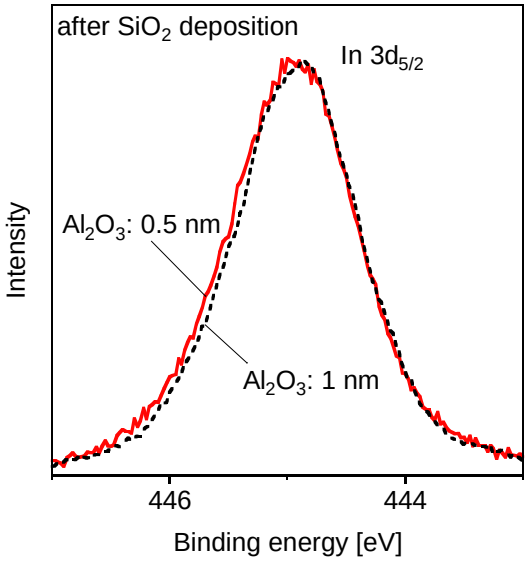
after SiO2 deposition
In 3d5/2
Intensity
Al2O3: 0.5 nm
Al2O3: 1 nm
446
444
Binding energy [eV]

Fig. 10.

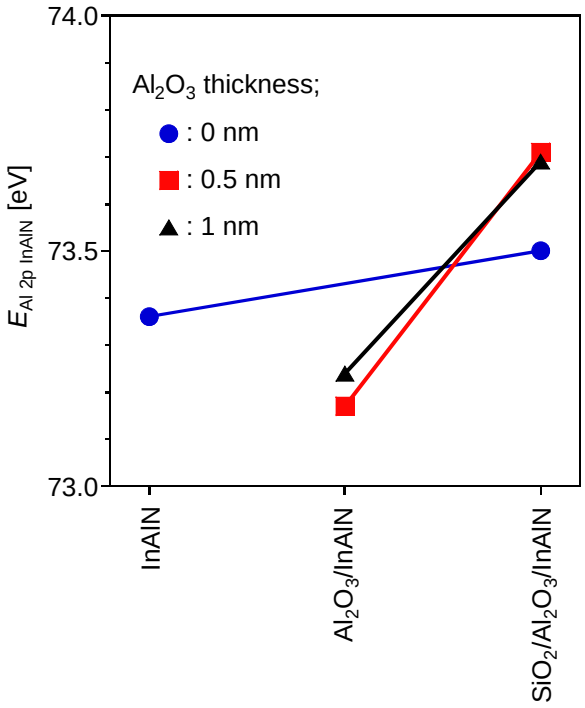
74.0
73.5
73.0
Al2O3 thickness;
: 0 nm
: 0.5 nm
: 1 nm
EAl 2p InAlN [eV]
InAlN
Al2O3/InAlN
SiO2/Al2O3/InAlN

Fig.11.

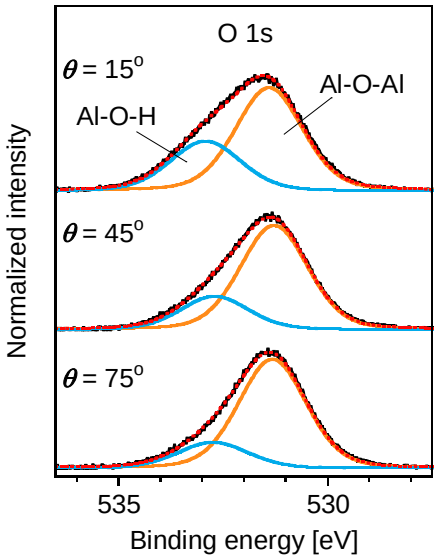
O 1s
θ = 15°
Al-O-H
Al-O-Al
θ = 45°
θ = 75°
Normalized intensity
535
530
Binding energy [eV]

Fig.12.